

Residual stress determination of silicon containing boron dopants in ceramic matrix composites

Michael W. Knauf¹  | Craig P. Przybyla² | Andrew J. Ritchey³ | Rodney W. Trice⁴ | R. Byron Pipes⁵

¹School of Aeronautics and Astronautics, Purdue University, West Lafayette, Indiana

²Air Force Research Laboratory, Wright-Patterson Air Force Base, Ohio

³Rolls-Royce Corporation, Indianapolis, Indiana

⁴School of Materials Engineering, Purdue University, West Lafayette, Indiana

⁵Schools of Aeronautics and Astronautics, Materials Engineering and Chemical Engineering, Purdue University, West Lafayette, Indiana

Correspondence: Michael W. Knauf, Arnold Air Force Base, TN 37389 (Michael.Knauf@us.af.mil)

Funding information

Research funding provided by US Air Force, materials provided by Rolls Royce.

Abstract

Raman spectroscopy was utilized to investigate residual stresses found within a SiC/SiC ceramic matrix composite containing Hi-Nicalon™ fibers, a slurry melt-infiltrated matrix of silicon carbide particles, and silicon matrix. Large gradients of electrically active boron are found throughout various regions within the crystalline lattice of the silicon matrix. The regions were identified by the varying degrees of asymmetry and peak width measured in the resonant Fano profile of the doped silicon. A methodology to determine the residual stress state of silicon exhibiting varying degrees of electrically active boron is presented by utilizing the changes in the Raman profile parameters. Previous works on similar SiC/SiC CMCs have attributed spatial gradients in the wavenumber to large fluctuations in stress. By applying the proposed methodology, we show that these observations are related to active boron that is segregated in various matrix areas. Utilizing this methodology, mean compressive stresses in various silicon regions were found to be approximately 300 MPa, with complementary tensile silicon carbide particle stresses of approximately 300 MPa.

1 | INTRODUCTION

Ceramic Matrix Composite (CMC) materials are poised to replace many traditionally metallic high-performance alloy components in hot sections of jet turbine engines, greatly increasing efficiency and available thrust.^{1,2} There are inherent difficulties in producing these materials, not least of which is controlling the levels of residual stress within the composite. The stresses come as a result of coefficient of thermal expansion mismatch between constituents, intrinsic stresses developed during chemical vapor infiltration,³ and possibly crystallization expansion of silicon

resulting from a significant volume increase in the phase transition from liquid to solid.⁴ To capitalize on the vast benefits of CMCs, the full residual stress state must be understood, predicted, and controlled. Various authors have experimentally determined residual stress states through Raman spectroscopy,^{4,5} X-ray diffraction,^{6–8} indentation,⁹ piezospectroscopic methods,¹⁰ and the common intersection point method.^{11–13} The reported stresses determined through these multiple techniques vary by orders of magnitude. Of the various methods available to study residual stresses, Raman spectroscopy requires relatively little material and provides spatial resolutions of 1 μm or less, making it an invaluable tool in stress determination at the microscopic level.¹⁴

Anastassakis et al^{15,16} developed a methodology to determine the stress in a silicon crystal by linearly correlating the level of strain within the material to the change

Based upon Knauf dissertation entitled “Effects of Heat Treatment on SiC-SiC Ceramic Matrix Composites,” Purdue University, 2017. Partially presented at 2018 United States Advanced Ceramics Association conference, Cape Canaveral, FL.

in the Raman characteristic wavenumber, $\Delta\omega$ (normally the peak center of a Lorentzian profile). Assuming the strain is lower than the elastic limit, this can then be correlated with the stress found within the constituents. Typically, the relationship between stress and change in wavenumber is reported directly. For many materials, this shift linearly corresponds to a change in the hydrostatic stress state of the constituent being interrogated. Depending on the known loading, this hydrostatic stress can be correlated with stress in distinct directions (e.g., uniaxial, biaxial, or hydrostatic).¹⁷ This methodology can also be applied to many crystalline materials, including CMC constituents such as polycrystalline silicon, silicon carbide, and Hi-NicalonTM fibers (Nippon Carbon, Tokyo, Japan).^{16,18,19}

Pure silicon exhibits a linear shift in peak location with applied stress for the peak nominally located at 520.5 cm^{-1} . This peak is triply degenerate, and remains degenerate with applied stress under normal circumstances. Therefore, only the hydrostatic component of the stress tensor (σ_H) can reliably be ascertained through Raman spectroscopy. When stressed, the wavenumber shifts according to Equation 1:

$$\Delta\sigma_H = \Delta\omega \times C, \quad (1)$$

where $C_{Si} = -0.177\text{ GPa cm}^{-1}$ for silicon.¹⁷ The 6H polytype of silicon carbide exhibits an analogous wavenumber shift of $C_{SiC} = -0.283\text{ GPa cm}^{-1}$ for the primary peak at 789 cm^{-1} with applied stress.¹⁸

Raman spectroscopy is considered a surface technique as most materials readily absorb and/or reflect the incident laser light within a few micrometers or less.²⁰ An absorption depth, δ , can be defined to compare the relative depths of penetration of a particular laser wavelength in different materials as $\delta = 1/\alpha$, where α is the absorption coefficient for the material. This is the depth at which the intensity of the incident light decreases by 63% ($1-1/e = 63\%$).²¹ Linear interpolation of silicon absorption coefficient values determined by Aspnes et al²² for a green 514.5 nm wavelength laser (such a laser was utilized in subsequent investigations) provides an absorption coefficient of approximately $15\,000\text{ cm}^{-1}$. Taking the reciprocal gives the effective depth of penetration of approximately $0.67\text{ }\mu\text{m}$ for this laser. Therefore, silicon measurements utilizing Raman spectroscopy are effectively a surface technique.

Silicon carbide, however, is relatively transparent to green 514.5 nm laser light. Linear interpolation of absorption coefficient data given by Derst et al²³ for crystalline SiC provides an absorption coefficient of approximately 14 cm^{-1} . The corresponding penetration depth is $710\text{ }\mu\text{m}$. This result has two repercussions; first, the stress measured by Raman spectroscopy in SiC has a volumetric element

and should not be modeled as a plane stress state (a common assumption in surface measurements). Second, it is possible to capture the Raman signature of the silicon matrix below any SiC particulates, and the stress state of this silicon will be three-dimensional as well.

Boron is a common additive (dopant) in silicon melt-infiltrated composites,²⁴ and has a major influence on many of the processes involved in residual stress measurement. Silicon dopants in groups IIIA and VA of the periodic table (including boron) introduce an asymmetric profile shape in the Raman signature, termed Fano resonance.^{25–27} This is due to the Fermi level (chemical potential of electrons) moving out of the semiconductor band gap and toward either the conduction band or the valence band of silicon, depending on the dopant used. Thus, these silicon dopants change the electronic structure of silicon and affect the Raman signature, estimated by a Fano line shape.^{27–29} The effects of the Fano resonance must be removed prior to stress determination to accurately measure the stress in silicon which contains group IIIA or VA elements. Fano resonance affects the silicon profile in several ways: (a) it introduces asymmetry to a normally symmetric Raman spectra; (b) the silicon peak center is shifted away from the normal stress-free silicon value of 520.5 cm^{-1} ; (c) it shifts the characteristic wavenumber even further from the stress-free value so that it no longer corresponds to the peak center as is the case for symmetric profiles; and (d) it increases the width of the spectra. Agaiby et al³⁰ utilized the asymmetry of the Fano profile to estimate the dopant concentration, and thus separate the wavenumber shift contributions of the boron dopant and stress state. The method employed by Agaiby et al was over a narrow range of dopant concentrations (up to $5 \times 10^{19}\text{ atoms/cm}^3$) and limited laser wavelengths (488, 514, and 633 nm). Chandrasekhar et al²⁷ noted the Fano profile asymmetry parameter is inconsistent between different laser wavelengths. Therefore, as an alternative, the spectra width can be used, which is relatively consistent between laser wavelengths, and literature provides much larger dopant concentration ranges for the stress-free wavenumber shift contributions.²⁷

In the current work, the residual stress state of a slurry melt-infiltrated ceramic matrix composite is studied using Raman spectroscopy. The material system is a Rolls-Royce composite produced with Hi-NicalonTM fibers woven into a five-harness satin weave, coated with boron nitride and silicon carbide, and subsequently infiltrated with silicon carbide particles and a boron-doped silicon matrix. The Fano effects on the silicon Raman signature caused by boron doping are separated from the Raman shift measured in the silicon phase induced by residual stress, thus providing accurate residual stress measurements for the silicon and silicon carbide constituents.

2 | EXPERIMENTAL PROCEDURE

2.1 | Sample preparation

Residual stress measurements were made on specimens cut from a 4 mm thick SiC/SiC slurry melt-infiltrated CMC plate. A surface grinder equipped with a diamond blade made initial cuts from the host plate, plunging at increments of 1 μm per pass with a water-based lubricant. Sectioning to various smaller sizes was performed using a low speed diamond cut-off saw (VC-50; LECO, St. Joseph, MI). One specimen was sectioned to 25 mm \times 25 mm \times 4 mm, while another was sectioned to 4 mm \times 3 mm \times 4 mm. The smaller sample size was required to investigate the viability of Raman spectroscopy for follow-on experiments in a high temperature heated stage which utilizes a small crucible. The Raman results for this small sample were compared with the results of the larger sample to validate that significant residual stresses were not released when machining the relatively small sample. All samples were polished using successive diamond polishing compounds of 6, 3, and 1 μm .

Stress-free reference samples were needed for the silicon as the published stress-free wavenumbers for pure silicon are invalid when Fano resonance is present (detailed in Discussion below). As part of the manufacturing process, the surface of the as-manufactured CMC plates had small globules of highly doped silicon that extend 1 mm or more past the bulk of the plate surface. The apex of these globules were assumed to be stress-free because they are relatively far from the fibers and other constituents which would produce residual stresses from CTE mismatch and silicon expansion upon freezing. Four suitable globules were polished using successive diamond polishing compounds of 6, 3, and 1 μm and investigated with Raman spectroscopy.

2.2 | Raman spectroscopy measurement procedure

The 514.5 nm line of an Ar+ laser (Stellar-REN; Stellar Pro, Centerville, Utah) was used with a Raman system (Renishaw inVia, Renishaw PLC, Wotton-under-Edge, UK) incorporating a backscattering arrangement. The Raman microscope was equipped with a grating of 1800 lines/mm, providing the required range to study both silicon and silicon carbide signatures in the same measurement. The laser power was kept to <2 mW at the sample to prevent heating issues from the laser while providing strong signal. Two accumulations, each 10 seconds long, were taken of each point. A laser spot size of approximately 1 μm was produced with a 100 \times objective. The Raman shift of a single-silicon crystal standard reference was used to calibrate the equipment.

Three areas of silicon were observed using the Raman system: underneath silicon carbide particles (which also produced a silicon carbide spectra because SiC is opaque to 514.5 nm light), on the surface of the matrix, and within the fiber tow. No fewer than 60 point measurements were taken of each area, including data from both the large and small as-received samples. Examples of the SiC particles and surface matrix microstructure are found in Figure 1, where the dark SiC particles are seen within a light-colored silicon matrix. Figure 2 illustrates the coated Hi-NicalonTM fibers with a centrally located silicon section. All measurements were randomly chosen throughout the central area of each specimen, and were centered in each feature as shown where the "X" marks a common example laser location. Finally, an intratow area (shown in Figure 3) was mapped in 1 μm steps utilizing the same Raman equipment.

2.3 | Residual stress determination

The Raman signatures of pure silicon and silicon carbide are represented by Lorentzian distributions,^{14–16,18} described by Equation 2,

$$I(\omega)_{i,\text{Lorentz}} = \frac{I_0}{\Gamma \left(1 + 4 \left(\frac{\omega - \omega_0}{\Gamma} \right)^2 \right)}, \quad (2)$$

where $I(\omega)$ is the functional value of the equation, I_0 is an arbitrary pre-multiplier, Γ is the full width of the peak at half of the maximum peak height (FWHM), ω_0 is the peak center, and ω is the abscissa.

The Fano line shape found in doped silicon can be described by Equation 3,

$$I(\omega)_{i,\text{Fano}} = \frac{I_0 \left(q + \left(\frac{\omega - \omega_0}{\Gamma} \right) \right)^2}{1 + \left(\frac{\omega - \omega_0}{\Gamma} \right)^2}, \quad (3)$$

where ω is the abscissa, q is the asymmetry parameter, ω_0 is the Fano wavenumber, Γ is the half width at half of the

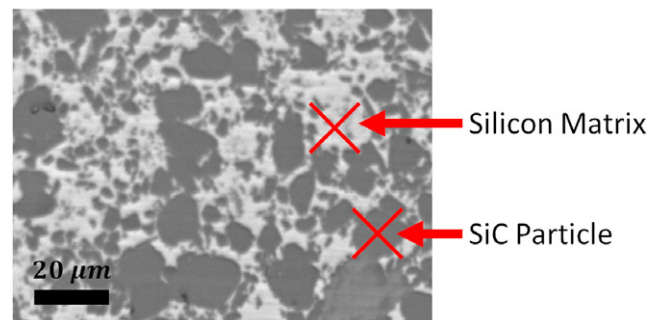


FIGURE 1 The dark gray particles are silicon carbide, while the light gray matrix is doped silicon. Example common Raman measurement locations are identified by X's: SiC particle/silicon underneath SiC particle; surface silicon [Color figure can be viewed at wileyonlinelibrary.com]

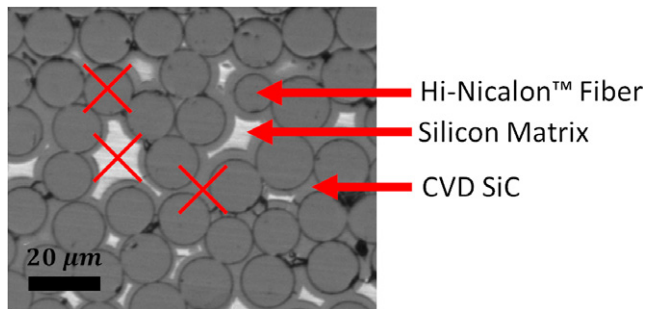


FIGURE 2 The dark gray circles are Hi-Nicalon™ fibers with a very dark overcoat of boron nitride, and an additional overcoat of silicon carbide. The intratow veins are filled with doped silicon (light gray) during the melt infiltration step [Color figure can be viewed at wileyonlinelibrary.com]

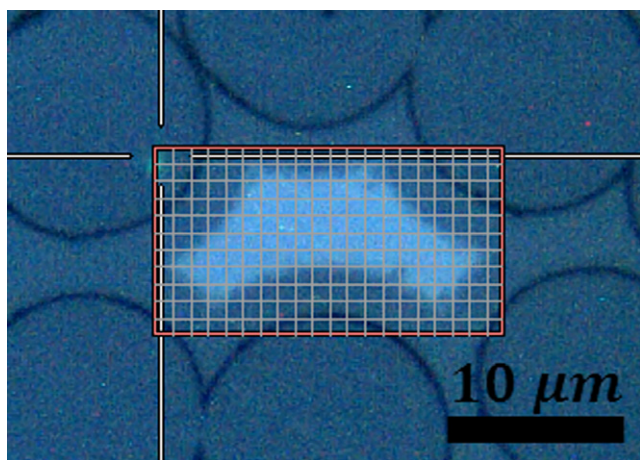


FIGURE 3 A Raman measurement map was investigated of an intratow area. Measurements were taken at each grid intersection, corresponding to 1 μm increments. Although indiscernible with visible light, Raman spectroscopy results of this mapping show large gradients in activated boron concentrations within the intratow silicon, as discussed below and found in Figure 9 [Color figure can be viewed at wileyonlinelibrary.com]

maximum peak height (as opposed to the full width at half of the maximum peak height used in the Lorentz equation), and I_0 is an arbitrary fitting constant. The peak position is offset from the characteristic wavenumber, ω_0 , to $\omega_0 + \Gamma/2q$. The Fano line shape approaches a Lorentzian in the limit of $q \rightarrow \infty$. The data points produced through Raman microscopy can be fitted with a summation of Lorentzian and Fano line shapes, along with a linear baseline, to determine the characteristic wavenumbers of the various peaks, as shown in Equation 4.

$$I_{\text{total}}(\omega) = \sum_{i=1}^n I(\omega)_i + A(\omega). \quad (4)$$

A curve represented by $I(\omega)_i$ is added for every peak (Lorentz or Fano) present in the spectra, $A(\omega)$ is the linear baseline, $I_{\text{total}}(\omega)$ is the overall functional value at the various data points, and ω is the abscissa. In this work,

the curve is fit using a nonlinear least squares MATLAB routine. By fitting the whole profile simultaneously, resulting parameters found through the fitting routine represent very accurate peak measurements (approximately $\pm 0.1 \text{ cm}^{-1}$).²⁰

3 | RESULTS AND DISCUSSION

3.1 | Dopant activation and stress measurement

For any dopant to affect the electronic characteristics of silicon, it must be electrically active. For boron, activation requires individual boron atoms to be covalently bonded to four silicon atoms as a substitutional atom in the overall silicon tetrahedral crystal lattice arrangement. This activation significantly reduces the resistivity of a silicon semiconductor, and is thus of interest to the semiconductor industry.³¹ Full activation is difficult to achieve. Precipitation of silicon borides in silicon causes electrical inactivity of boron due to boron atoms being absorbed by SiB_x structures.³² Alternatively, boron can form interstitial clusters which can render many boron atoms inactive within silicon.²⁹ These clusters have the ability to dissolve at temperatures $>850^\circ\text{C}$.³³ In addition, the manufacturing environment can also lead to boron deactivation, as in the case of hydrogen saturating one of the four tetrahedral silicon bonds.³¹ Finally, compressive strains at high temperatures have also been found to increase the amount of substitutional boron within the silicon lattice, while tensile strains decrease the amount of boron dissolved.^{29,34}

Chandrasekhar et al²⁷ determined that a Fano-type Raman spectroscopy resonance profile replaces the normally Lorentzian profile of silicon at 520.5 cm^{-1} for boron-doped silicon. This is due to the Fermi level entering the valence band of highly p-doped silicon at boron concentrations greater than approximately $10^{19} \text{ atoms/cm}^3$ at room temperature, producing a degenerate semiconductor. Localized vibrational modes also appear as Fano line shapes at $\sim 620 \text{ cm}^{-1}$ and $\sim 644 \text{ cm}^{-1}$ as a result of doping. The former is attributed to the ^{11}B isotope, while the latter is attributed to the ^{10}B isotope. The intensities of the two peaks follow that of boron's natural isotope occurrence, namely 80% is found as ^{11}B and 20% is found as ^{10}B . In the same study, Chandrasekhar also determined that the width and asymmetry of the primary Fano profile is dependent upon the dopant concentration. The asymmetry is additionally dependent on the laser wavelength used, while the width is relatively constant between different wavelengths. The proposed technique utilizes this information to determine the stress free wavenumber as a function of peak half width to correct for boron concentration. These values are summarized for a 514.5 nm laser in Table 1.

TABLE 1 Tabulated Fano parameters of boron-doped silicon,²⁴ extended with this work

Dopant Concentration (atoms/cm ³)	Asymmetry parameter (<i>q</i>)	Width parameter (Γ , cm ⁻¹)	Fano wavenumber (ω_0 , cm ⁻¹)
1.5×10^{19}	N/A ^a	2.88	520.2
6×10^{19}	N/A ^a	6.2	519.7
1.5×10^{20}	N/A ^a	8.85	515.7
4×10^{20}	2.57	11.8	511
N/A ^b	1.70	14.20	505

^aAsymmetry parameters are missing for the lowest concentrations as the Chandrasekhar values were not obtained with a 514.5 nm laser.

^bThe highest dopant concentration is unknown (other parameters determined through this work).

Asymmetry parameters are missing in the table because they are dependent on the wavelength of the laser.

This work primarily uses the stress-free Fano parameter values from the work of Chandrasekhar et al; however, the dopant concentrations found in the CMC under investigation are greater than the maximum concentrations found in literature. Therefore, additional stress-free silicon parameters are required to more fully populate Chandrasekhar's data.²⁷ Raman spectra of the globules mentioned previously were acquired for both an as-received plate and a heat-treated plate. The heat treatment was performed at 1300°C for one hour in a carbon furnace under an argon atmosphere. The mean wavenumbers decreased considerably from the as-received to the heat-treated plate, from 508.92 to 506.42 cm⁻¹. The asymmetry parameter, *q*, also decreased (became more asymmetric), and the peak half width value increased. These behaviors indicate an increase in the boron activation level.²⁷ Both the as-received and heat-treated values indicate higher activated boron levels than those found in literature (although the actual dopant concentration is unknown). Therefore, the parameters determined from these fits can be utilized in extending the Chandrasekhar parameters into higher boron activation concentrations than those found in literature. Figure 4 illustrates the extreme asymmetry found in the heat-treated panel globules. This particular point has a Fano wavenumber of 506.39 cm⁻¹, a half-width of 12.96 cm⁻¹, and an asymmetry parameter of 1.84. The closed circle data points are from the experimental measurement, the bold "Profile Fit" line is the overall summation of the fit, the various broken lines are the components of the overall fit, and the open circles are the residuals between the experimental data and the curve fit. It should be noted the Fano effect on most silicon profiles was not this extreme, but exhibited more subdued Fano characteristics and could often be mistaken for a Lorentzian curve.

Figure 5 plots the Fano wavenumber vs half-width for the as-received (AR, open circles) and heat-treated (HT,

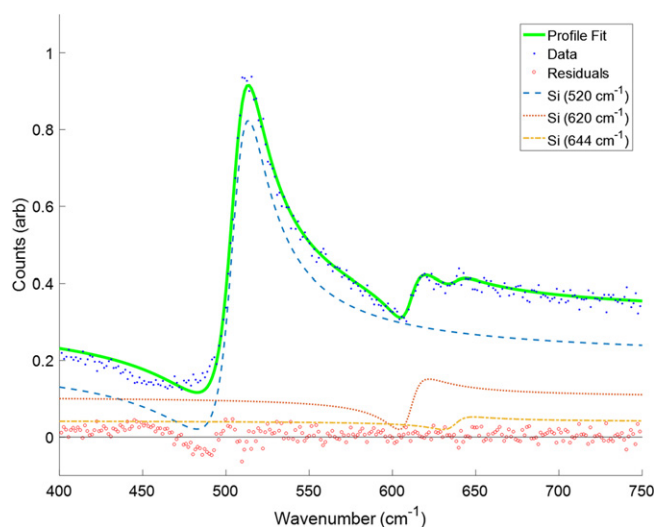


FIGURE 4 Plot of Raman spectra as a function of wavenumber for an individual silicon globule after heat treatment found on the outer face of a CMC plate. This profile exhibits very high asymmetry, very large peak width, and a peak at 509.91 cm⁻¹, which is shifted considerably from undoped and unstressed silicon. The characteristic Fano wavenumber is shifted further still, to approximately 506.39 cm⁻¹. Two additional peaks are seen around 620 and 644 cm⁻¹, which correspond to the boron isotopes ¹¹B and ¹⁰B, respectively [Color figure can be viewed at wileyonlinelibrary.com]

open squares) globules. Values from Table 1 are also plotted, with linear interpolations in-between the values. Finally, a least-squares fit was performed on the current dataset to build an extension for higher levels of dopant, fixing the fitted line to the highest-doped Chandrasekhar data point.²⁷ Although the dopant level is unknown, large dopant gradients are found throughout the silicon matrix by observing the increase in Fano half-width with decreasing Fano wavenumber. The resulting line can be used for stress estimation in further analyses. A similar exercise was performed to determine an appropriate asymmetry value at high dopant levels for a 514.5 nm laser wavelength. The extended values determined from these analyses, along with tabulated Chandrasekhar values for a 514.5 nm laser, are given in Table 1.

The three areas investigated (silicon beneath silicon carbide particles, silicon on the surface of the material, and silicon in between fibers within a transverse fiber tow) exhibited varying Fano profile parameters, with consistent trends between each particular area. The silicon found beneath silicon carbide particles was found to have the least amount of activated boron, and thus the Raman signature had the least asymmetry, smallest half-width, and least deviation from the pure silicon stress-free characteristic Raman wavenumber of 520.5 cm⁻¹, shown as open circles in Figure 6. The silicon found directly in the center of

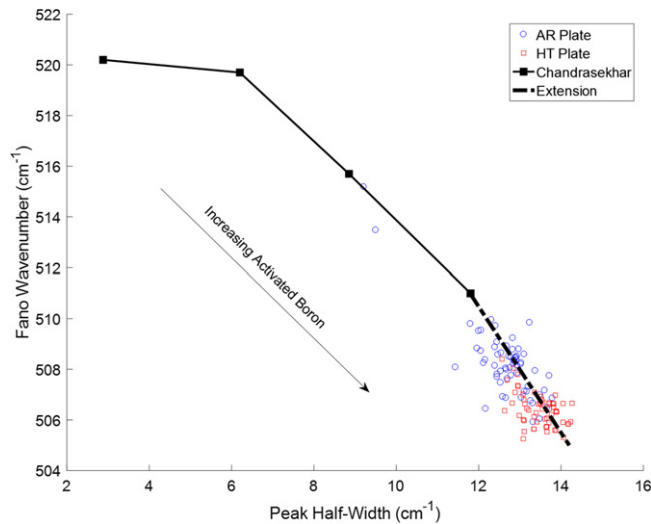


FIGURE 5 Plot of the stress-free wavenumber vs peak half-width values developed by Chandrasekhar,²⁷ illustrating the measurements taken to build an extension to these data. The circles and squares represent stress-free measurements taken from silicon globules from a CMC plate that was in the as-received and heat-treated conditions, respectively. A best-fit extension was produced using a least-squares fitting routine. Increasing peak half width and decreasing wavenumbers are indicative of increasing activated boron in silicon [Color figure can be viewed at [wileyonlinelibrary.com](#)]

various fibers showed the greatest amount of activated boron, having the largest half-widths, and also the largest deviation from pure silicon, shown as open triangles in Figure 6. Finally, the surface silicon displayed varying amounts of activated boron, as indicated by the very large range of wavenumbers and half-width values, and are shown as open squares in Figure 6. When plotted as characteristic wavenumber vs half-width, along with the extended Chandrasekhar values, the Fano wavenumbers were found to follow the Chandrasekhar/experimentally extended stress-free curve and were nearly always slightly above this stress-free line, an indication that the silicon is under a compressive state of stress.

The general methodology developed by Anastassakis et al^{16,17} to determine the residual stress state relies solely on the difference between the stress-free reference and the stressed material. Obviously, this methodology results in critical errors for doped silicon stress determination. By determining the difference between a stress-free interpolated line and each data point, an accurate stress reading can be produced. In this way, the current methodology extends that of Anastassakis by determining the stress-free wavenumber as a function of peak half-width to account for active boron.

Utilizing the stress-free lines in the wavenumber vs half-width plot above, the following methodology is applied to every measurement:

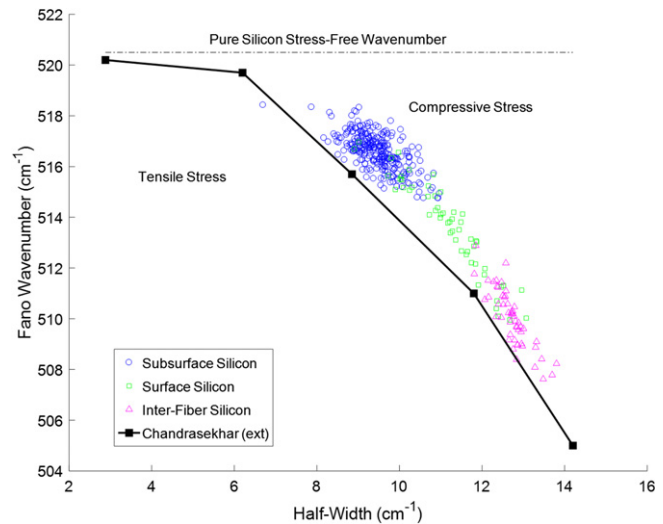


FIGURE 6 Various as-received silicon wavenumbers vs half-width parameters are shown. Large gradients of activated boron are found throughout the various microstructural CMC matrix areas. Without accounting for the activated boron, the upper “Pure Silicon Stress-Free Wavenumber” dotted line would be utilized to determine if stresses were compressive (above the line) or tensile (below the line). By utilizing the Fano half-width parameter, stressed measurements found below the bold extended Chandrasekhar curve are in a tensile stress state, while stressed measurements above the curve are in a compressive state [Color figure can be viewed at [wileyonlinelibrary.com](#)]

1. The fitting routine outputs the characteristic Fano wavenumber, the half-width parameter, and the asymmetry parameter for each Raman spectra recorded.
2. The stress-free wavenumber at this half-width is determined through linear interpolation of the respective stress-free lines.
3. The difference in wavenumber between the stress-free wavenumber and the wavenumber of the measured point is determined.
4. The wavenumber difference is converted to a stress value through the standard Anastassakis wavenumber to hydrostatic stress relationship, as found in Equation 1.

3.2 | Central intratow silicon stress

Scans were collected directly on the center of the silicon found in-between fibers. These points displayed very high asymmetry of the Fano profile, indicating very high levels of activated boron within these areas. Sixty single-point intratow measurements are shown as open triangles in Figure 6. Utilizing the methodology from above, the as-received hydrostatic stress is found to be in compression, with a mean of -240 MPa and a standard deviation of 100 MPa. The mean standard error is 0.13 cm^{-1} , which corresponds to 20 MPa (using Equation 1). The standard error incorporates

both the Anastassakis¹⁶ uncertainty value ($\pm 0.05 \text{ cm}^{-1}$) and the uncertainty due to the numerical fitting routine.³⁵

3.3 | Subsurface silicon stress

Sub-surface silicon measurements are shown to exhibit the least amount of activated boron, as evidenced by the relatively low Fano half-width of the silicon profiles open circles in Figure 6. This is due to a combination of the high laser absorption found in silicon (the laser interrogates only a few hundred nanometers into the silicon) as well as boron-depletion in silicon near SiC grain boundaries. When the laser light travels through the silicon carbide particle, the first silicon the light encounters touches the SiC particle grain. These silicon areas consistently show depletion of activated boron. The depletion zones represent either a lack of boron atoms entirely or a lack of electrically active boron atoms, with Raman spectroscopy being unable to distinguish between these two cases.

The mean hydrostatic stress in subsurface silicon is found to be 330 MPa in compression. This is due to the higher CTE of silicon carbide than that of silicon, which produces an overall compressive state of stress in the silicon while a tensile stress state is found in the SiC to equilibrate the stress levels.^{36–38} The standard deviation of these stresses is 120 MPa. The mean standard error due to fitting is 0.085 cm^{-1} , which corresponds to 15 MPa.

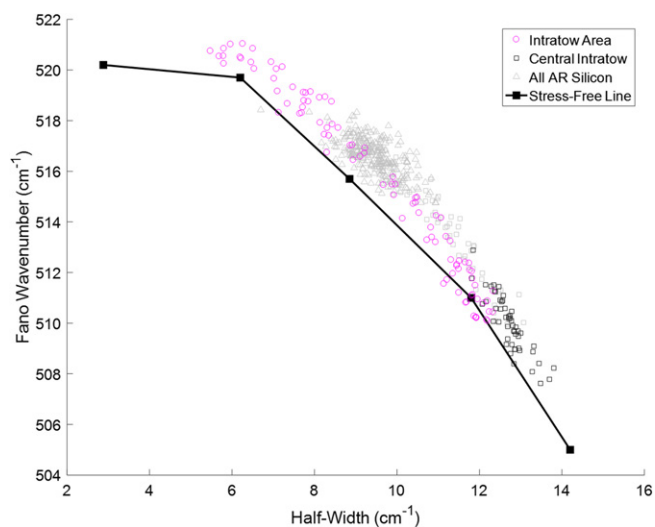


FIGURE 7 The central portion of each intratow region had very high levels of boron activation, as shown by the open squares above. However, when measurements were taken throughout an entire intratow area, large gradients of boron were found to exist, as indicated by the circles covering a large range of Fano wavenumbers and half-widths. The remaining as-received silicon data are shown by the squares as reference [Color figure can be viewed at wileyonlinelibrary.com]

The silicon carbide Raman signatures were analyzed by fitting three peaks to the α -SiC peaks around 767, 789, and 797 cm^{-1} . The most intense peak (at 789 cm^{-1}) was utilized to determine the residual stress state using the normal methodologies.¹⁸ The silicon carbide particles were determined to exhibit an average hydrostatic residual tensile stress of approximately 300 MPa with a standard deviation of approximately 240 MPa.

3.4 | Silicon found on the surface of the matrix

An additional silicon area investigated by Raman spectroscopy is the silicon found in-between silicon carbide particles in the overall matrix. These areas are found to exhibit very large gradients of activated boron, as shown through the variation in half-width parameter seen in the open squares in Figure 6. This figure illustrates the large activated dopant distributions generated through the manufacturing process of this material. A standard error of 0.085 cm^{-1} , corresponding to 15 MPa, was determined from the fitting statistics. Measurements were often taken relatively far from silicon carbide grain boundaries, and thus boron-depleted zones are less common in these measurements. The mean hydrostatic stress is 320 MPa in compression with a standard deviation of 100 MPa, similar to that of the subsurface silicon measurements.

3.5 | Silicon found throughout intratow region

A single area scan of an intratow region was taken to observe stress gradients within the silicon. A representative area is found in Figure 3, where the light-colored center is silicon, the outer dark region is the fiber/Chemical Vapor Infiltrated (CVI) SiC area, and the intersections of the light lines represent the locations of each measurement. Through observation of the Fano half-width, analysis of this area showed significant gradients of activated boron within these regions, with boron depletion evident near the CVI SiC. This is similar to the boron depletion found behind the SiC particles mentioned previously. This is either a product of a boron segregation/boundary layer effect during melt infiltration or due to boron becoming trapped in an electrically inactive state near the grain boundaries.^{29,39,40} In the case of boron segregation, boron atoms would physically not be in the silicon lattice in these areas, likely being robbed by small silicon boride precipitates. In the case of boron entrapment, boron atoms would be present but would not be electrically active. The two cases are indistinguishable with Raman spectroscopy.

Figure 7 subdues (shown as open triangles) the previously graphed data points for the subsurface and surface

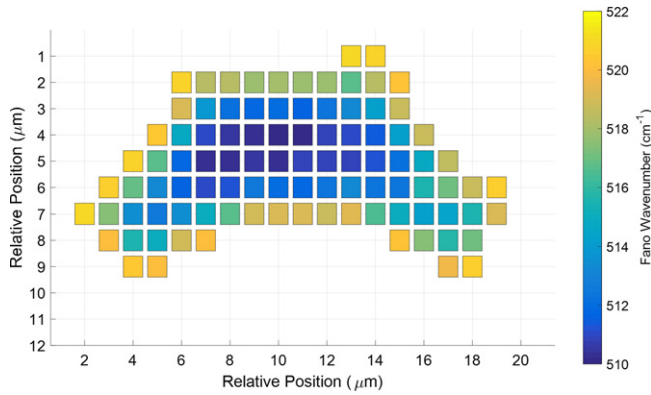


FIGURE 8 Fano wavenumber results of intratow area scan shown in Figure 3 at room temperature. Very low wavenumbers in the center are indicative of either high tensile stresses or high concentrations of activated boron. Additional parameters from the Raman spectra are required to determine the stress state. Measurements taken in 1 μm intervals [Color figure can be viewed at wileyonlinelibrary.com]

silicon, and the stress-free line is shown connecting the square Table 1 values. The intratow region Fano wavenumbers vs half-widths are shown as open circles. Note that these data were not shown in previous figures. The central intratow values previously determined are shown as open squares as comparison. The central values in the area scan were similar to the central values found earlier, while there are obvious large gradients in the activated boron concentration.

Figure 8 displays the map of Fano wavenumber in the interrogated intratow area shown in Figure 3. The wavenumber are functions of the boron activation level, and thus the wavenumbers are lowered considerably as the

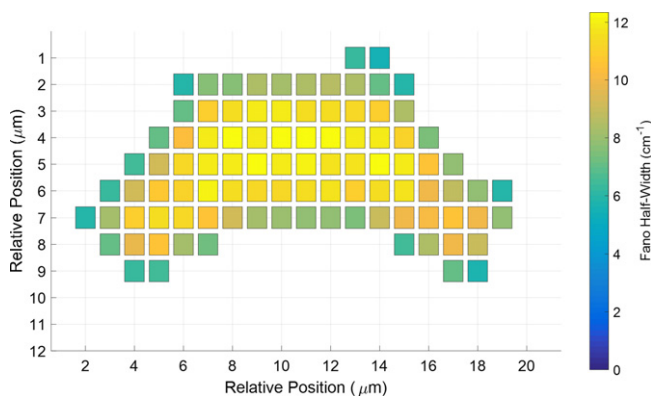


FIGURE 9 Fano half-width parameter results of intratow area scan shown in Figure 3 at room temperature (determined from the same scan data as Figure 8). The large peak widths, especially near the center, are indicative of high concentrations of boron dopant within the silicon [Color figure can be viewed at wileyonlinelibrary.com]

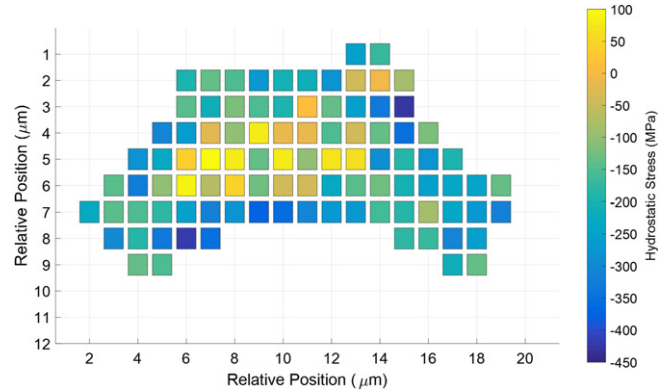


FIGURE 10 The Fano wavenumber and half-width must be utilized collectively to determine the stress state at each measurement point, as shown in the figure above. Hydrostatic stresses in this sample ranged between 425 MPa in compression to 90 MPa in tension, with an average value of 180 MPa in compression [Color figure can be viewed at wileyonlinelibrary.com]

activated boron increases near the center of the silicon vein. This phenomenon of decreased wavenumbers far from grain boundaries mimics the behavior of results from Jannotti et al;⁴¹ however, Jannotti did not take the half-width or asymmetry of the reported Fano profiles into account, and reported large tensile stresses in these central areas that are likely to have been an erroneous interpretation of the data. Figure 9 displays the half-width of the Fano profiles per the investigated points of the area scan, which qualitatively illustrates the boron activation levels of the various points. Finally, Figure 10 illustrates the corrected stress distribution within the intratow area under investigation.

Hydrostatic stresses ranged from 425 MPa in compression to 90 MPa in tension, with an average value of 180 MPa in compression and a standard deviation of 120 MPa. Large stress variations are expected due to the small laser spot size investigating local stress values.²⁰ Hi-Nicalon fibers have a lower CTE than silicon,^{42,43} and thus

TABLE 2 Summary of silicon and silicon carbide hydrostatic stresses

Measured area	Mean silicon hydrostatic compressive stress, MPa	Mean silicon carbide hydrostatic tensile stress, MPa
Central intratow	240	—
SiC particle/subsurface silicon	330	300
Surface silicon	320	—
Intratow general area	170	—

the proximity of this investigated silicon to the fibers is likely affecting this stress state to be in overall less compression than other silicon found throughout the composite. However, very large incorrect tensile stresses (up to ~2 GPa) would have been calculated had the Fano parameters not been taken into account. Stresses in the silicon matrix phase and silicon carbide (when applicable) are summarized in Table 2 for all cases studied.

4 | CONCLUSIONS

Activated boron concentration levels must be incorporated into stress determinations to accurately describe the decreased silicon wavenumbers found in doped silicon. Without incorporation of these effects, the stresses determined through Raman spectroscopy will be more tensile than reality and will lead to exceptionally large standard deviations of stress. In addition, activated boron is found to be depleted near silicon carbide grain boundaries due to grain boundary segregation or electrical inactivation. Silicon stresses in between fibers within fiber tows exhibited considerably less compressive stress than the silicon stresses found in the general matrix areas due to the low CTE values of Hi-Nicalon fibers vs silicon. The mean intratow silicon stress throughout the entire intratow silicon vein area is approximately 180 MPa in compression, while the silicon mean compressive hydrostatic stresses in the general matrix areas are approximately 300 MPa.

ORCID

Michael W. Knauf  <http://orcid.org/0000-0003-1418-5651>

REFERENCES

- Ohnabe H, Masaki S, Onozuka M, Miyahara K, Sasa T. Potential application of ceramic matrix composites to aero-engine components. *Compos Part A Appl Sci Manuf*. 1999;30(4):489–96.
- Singh Y, Mansour R, Morscher G. Combined acoustic emission and multiple lead potential drop measurements in detailed examination of crack initiation and growth during interlaminar testing of ceramic matrix composites. *Compos Part A Appl Sci Manuf*. 2017;97:93–9.
- Choi D, Shinavski R, Steffier W, Spearing S. Residual stress in thick low-pressure chemical-vapor deposited polycrystalline SiC coatings on Si substrates. *J Appl Phys*. 2005;97(7):074904.
- Wing B, Halloran J. Microstress in the matrix of a melt-infiltrated SiC/SiC ceramic matrix composite. *J Am Ceram Soc*. 2017;100(11):5286–94.
- Wing B, Esmonde-White F, Halloran J. Microstress in reaction-bonded SiC from crystallization expansion of silicon. *J Am Ceram Soc*. 2016;99(11):3705–11.
- Bobet J, Lamon J. Study of thermal residual stresses in ceramic matrix composites. *J Alloys Compd*. 1997;259:260–4.
- Ramirez-Rico J, Stolzenburg F, Almer J, Routbort J, Singh D, Faber K. In situ imaging and strain determination during fracture in a SiC/SiC ceramic matrix composite. *Scr Mater*. 2013;69(7):497–500.
- Harder B, Almer J, Weyant C, Lee K, Faber K. Residual stress analysis of multilayer environmental barrier coatings. *J Am Ceram Soc*. 2009;92(2):452–9.
- Peitl O, Serbena F, Mastelaro V, Zanutto E. Internal residual stress measurements in a bioactive glass-ceramic using vickers indentation. *J Am Ceram Soc*. 2010;93(8):2359–68.
- Ma Q, Clarke D. Piezospectroscopic determination of residual stresses in polycrystalline alumina. *J Am Ceram Soc*. 1994;77(2):298–302.
- Morscher G, Gordon N. Acoustic emission and electrical resistance in SiC-based laminate ceramic composites tested under tensile loading. *J Eur Ceram Soc*. 2017;37(13):3861–72.
- Mei H. Measurement and calculation of thermal residual stress in fiber reinforced ceramic matrix composites. *Compos Sci Technol*. 2008;68(15):3285–92.
- Dassios K, Matikas T. Residual stress-related common intersection points in the mechanical behavior of ceramic matrix composites undergoing cyclic loading. *Exp Mech*. 2013;53:1033–8.
- De Wolf I. Micro-Raman spectroscopy to study local mechanical stress in silicon integrated circuits. *Semicond Sci Technol*. 1996;11(2):139–54.
- Anastassakis E, Pinczuk A, Burstein E. Effect of static uniaxial stress on the Raman spectrum of silicon. *Solid State Commun*. 1969;8(2):133–8.
- Anastassakis E, Cantarero A, Cardona M. Piezo-Raman measurements and anharmonic parameters in silicon and diamond. *Phys Rev B Condens Matter*. 1990;41(11):7529–35.
- Anastassakis E. Strain characterization of polycrystalline diamond and silicon systems. *J Appl Phys*. 1999;86(1):249–58.
- DiGregorio J, Furtak T. Analysis of residual stress in 6H-SiC particles within Al₂O₃/SiC composites through Raman spectroscopy. *J Am Ceram Soc*. 1992;75(7):1854–7.
- Gouadec G, Colomban P, Bansal NP. Raman study of Hi-Nicalon fiber reinforced celsian composites: II, residual stress in fibers. *J Am Ceram Soc*. 2001;84(5):1136–42.
- Withers P, Bhadeshia H. Residual stress, Part 1 - Measurement techniques. *Mater Sci Technol*. 2001;17:355–64.
- Brown M, Arnold C. Fundamentals of laser-material interaction and application to multiscale surface modification. In: Sugioka K, Meunier M, Piqué A, editors. *Laser precision microfabrication*. Berlin, Heidelberg: Springer; 2010: p. 91–120.
- Aspnes D, Studna A. Dielectric functions and optical parameters of Si, Ge, GaP, GaAs, GaSb, InP, InAs, and InSb from 1.5 to 6.0 eV. *Phys Rev B Condens Matter*. 1983;27(2):985–1009.
- Derst G, Wilbertz C, Bhatia K, Krätschmer W, Kalbitzer S. Optical properties of SiC for crystalline/amorphous pattern fabrication. *Appl Phys Lett*. 1989;54(18):1722–4.
- Suyama S, Kameda T, Itoh Y. Effect of structure of interfacial coating layer on mechanical properties of continuous fiber reinforced reaction sintered silicon carbide matrix composite. *J Mater Sci*. 2002;37(6):1101–6.
- Fano U. Effects of configuration interaction on intensities and phase shifts. *Phys Rev*. 1961;124(6):1866–78.
- Cerdeira F, Fjeldly R, Cardona M. Raman study of the interaction between localized vibrations and electronic excitations in boron-doped silicon. *Phys Rev B*. 1974;9(10):4344–50.

27. Chandrasekhar M, Chandrasekhar H, Grimsditch M, Cardona M. Study of the localized vibrations of boron in heavily doped Si. *Phys Rev B Condens Matter*. 1980;22(10):4825–33.
28. Nickel N, Lengsfeld P, Sieber I. Raman spectroscopy of heavily doped polycrystalline silicon thin films. *Phys Rev B Condens Matter*. 2000;61(23):558–61.
29. Pichler P. *Intrinsic Point Defects, Impurities, and Their Diffusion in Silicon*. Vienna, Austria: Springer; 2004.
30. Agaiby R, Becker M, Thapa S, Urmoneit U, Berger A, Gawlik A, et al. Stress and doping uniformity of laser crystallized amorphous silicon in thin film silicon solar cells. *J Appl Phys*. 2010;107(5):054312.
31. Cerofolini G, Meda L. *Physical Chemistry of in and on Silicon*. Berlin. Heidelberg. New York. London. Paris. Tokyo: Springer Science & Business Media; 2012.
32. Fahey P, Griffin P, Plummer J. Point defects and dopant diffusion in silicon. *Rev Mod Phys*. 1989;61(2):289–388.
33. Aboy M, Pelax L, Barbolla J, Duffy R, Venezia V. Boron activation and redistribution during thermal treatments after solid phase epitaxial regrowth. *Mater Sci Eng B*. 2005;124:205–9.
34. Sadigh B, Lenosky T, Caturla M, Quong A, Benedict L, Diaz de la Rubia T, et al. Large enhancement of boron solubility in silicon due to biaxial stress. *Appl Phys Lett*. 2002;80(25):4738–40.
35. Montgomery D. *Design and Analysis of Experiments*. 6th ed. New York, NY: John Wiley & Sons; 2004.
36. Okada Y, Tokumaru Y. Precise determination of lattice parameter and thermal expansion coefficient of silicon between 300 and 1500K. *J Appl Phys*. 1984;56(2):314–20.
37. Li Z, Bradt R. Thermal expansion of the hexagonal (6H) polytype of silicon carbide. *J Am Ceram Soc*. 1986;69(12):863–6.
38. Inoue Z, Kurachi Y. Structure change of SiC at high temperature. *Paper presented at: ISCCE 1983. Proceedings of the International Symposium on Ceramic Components for Engines*; 1983; Tokyo.
39. Sim B, Kim K, Lee H. Boron segregation control in silicon crystal ingots grown in Czochralski process. *J Cryst Growth*. 2006;290(2):665–9.
40. Burton J, Prim R, Slichter W. The distribution of solute in crystals grown from the melt. Part I. Theoretical. *J Chem Phys*. 1953;21(11):1987–91.
41. Jannotti P, Subhash G, Zheng J, Halls V. Measurement of micro-scale residual stresses in multi-phase ceramic composites using Raman spectroscopy. *Acta Mater*. 2017;129:482–91.
42. Katoh Y, Ozawa K, Shih C, Nozawa T, Shinavski R, Hasegawa A, et al. Continuous SiC fiber, CVI SiC matrix composites for nuclear applications: properties and irradiation effects. *J Nucl Mater*. 2014;448(1):448–76.
43. Corman G, Luthra K, Jonkowski J, Mavec J, Bakke P, Haught D, et al. Melt infiltrated ceramic matrix composites for shrouds and combustor liners of advanced industrial gas turbines. General Electric Company; 2011.

How to cite this article: Knauf MW, Przybyla CP, Ritchey AJ, Trice RW, Pipes RB. Residual stress determination of silicon containing boron dopants in ceramic matrix composites. *J Am Ceram Soc*. 2019;102:2820–2829. <https://doi.org/10.1111/jace.15942>